

Performance of VERA in 10 micro-arcsecond astrometry

Takumi NAGAYAMA,^{1,*} Hideyuki KOBAYASHI,^{2,3} Tomoya HIROTA,^{2,3}
Mareki HONMA,^{1,3} Takaaki JIKE,^{1,3} Mi Kyoung KIM,¹ Akiharu NAKAGAWA,⁴
Toshihiro OMODAKA,⁴ Tomoaki OYAMA,¹ Daisuke SAKAI,¹
Katsunori M. SHIBATA,^{2,3} and Yoshiaki TAMURA^{1,3}

¹Mizusawa VLBI Observatory, National Astronomical Observatory of Japan, 2-12 Hoshigaoka-cho, Mizusawa-ku, Oshu, Iwate 023-0861, Japan

²Mizusawa VLBI Observatory, National Astronomical Observatory of Japan, 2-21-1 Osawa, Mitaka, Tokyo 181-8588, Japan

³Department of Astronomy, School of Physical Sciences, The Graduate University for Advanced Studies, SOKENDAI, 2-21-1 Osawa, Mitaka, Tokyo 181-8588, Japan

⁴Graduate School of Science and Engineering, Kagoshima University, 1-21-35 Korimoto, Kagoshima, Kagoshima 890-0065, Japan

*E-mail: takumi.nagayama@nao.ac.jp

Received 2020 January 15; Accepted 2020 April 6

Abstract

Very Long Baseline Interferometry (VLBI) astrometry using the phase-referencing technique remains an open issue for the quantitative characterization of the observing conditions to achieve a feasible parallax precision of 10 micro-arcseconds (μas). To address this issue, we evaluated the astrometric performance of the VLBI Exploration of Radio Astrometry (VERA) through the parallax measurements of five distant star-forming regions under good observing conditions of close separations ($0.5\text{--}1.3^\circ$) and high elevations ($\geq 50^\circ$). Their parallaxes measured $89\text{--}200\ \mu\text{as}$, corresponding to distances of $5\text{--}11\ \text{kpc}$ with an error of $11\text{--}20\ \mu\text{as}$. Furthermore, we investigated the contributions to the position error budget and concluded that the tropospheric residual contribution is the dominant error source. We also confirmed that the astrometric error propagation strongly depends on the term $\Delta \sec Z$, which stands for the difference between $\sec Z$ of the target and its reference source, where Z is the zenith angle during the observations. We found that for a source pair with a $\Delta \sec Z$ less than 0.01 (for example, a set of a close separation of $\leq 0.5^\circ$ and a high elevation of $\geq 50^\circ$), we can achieve the parallax precision of $10\ \mu\text{as}$ using a typical monitoring program comprising 10 observing epochs over a span of two years.

Key words: astrometry — parallaxes — techniques: high angular resolution

1 Introduction

Very Long Baseline Interferometry (VLBI) astrometry using the phase-referencing observations is ongoing to measure the parallax of Galactic maser sources at the 10 micro-arcsecond (μas) level with VLBI Exploration of Radio Astrometry (VERA) and Very Long Baseline Array (VLBA) (e.g., Honma et al. 2012; Reid et al. 2019). It is well known that the VLBI astrometric precision ($\Delta\theta$) of the single baseline is expressed as $\Delta\theta \approx c\Delta\tau \cdot \theta_{\text{SA}}/D$, and can be improved by observing the close separation angle source (θ_{SA}) with the long baseline length (D) under the accurate delay calibration ($c\Delta\tau$) (Honma et al. 2010; Reid & Honma 2014). However, the astrometric precision of the VLBI array consisting of multiple baselines is complex and cannot be calculated analytically (Pradel et al. 2006; Asaki et al. 2007). Therefore, the exact observing condition required to achieve a parallax precision of 10 μas is quantitatively unclear. VLBI astrometry still remains an open issue.

VERA is a Japanese VLBI array consisting of four stations with baseline lengths ranging from a minimum of 1200 km to a maximum of 2300 km corresponding to a beam size of 1 milli-arcsecond (mas) at a frequency of 22 GHz (Kobayashi et al. 2003). VERA is dedicated to the phase-referencing astrometry with a dual-beam receiving system that can simultaneously observe the target and reference sources at separation angles in the range of 0.3–2.2 to effectively cancel the tropospheric fluctuations (Kawaguchi et al. 2000; Honma et al. 2003). In the phase-referencing observations, the phase delay is basically calibrated using the position reference radio sources, and it is fundamental to calibrate additional delay terms, such as those caused by excess delay errors introduced by the propagation medium effects through the troposphere and ionosphere, errors in the station coordinates, and errors of an instrumental nature, precisely. In VLBI astrometry at a separation angle in the range of 1°–2°, the systematic position error caused by these calibration errors is larger than the formal position error caused by the thermal noise (Hachisuka et al. 2006; Honma et al. 2007; Nagayama et al. 2015); therefore, the accurate calibrations of the abovementioned four components are fundamental to achieve a high astrometric precision.

Hence, the tropospheric zenith delay measured by the Global Positioning System (GPS) (Honma et al. 2008b), the ionospheric Total Electron Content (TEC) of the CODE's Global Ionosphere Map (GIM),¹ the station position measured by the monthly geodetic VLBI observations (Jike et al. 2009, 2018), and the instrumental delay between the dual-beam system measured by the horn-on-dish method

Table 1. Theoretical estimation of astrometric-position errors for a single baseline and a single epoch at the observing frequency of 22 GHz.*

Error source	Position error (μas)					
	1°	1°	1°	2°	2°	2°
Separation	1°	1°	1°	2°	2°	2°
Elevation	30°	50°	70°	30°	50°	70°
Troposphere	108	34	12	217	69	24
Ionosphere	24	11	4	48	22	9
Station position	8	8	8	16	16	16
Instrument	9	9	9	9	9	9
Thermal noise	17	17	17	17	17	17
RSS	113	41	24	224	76	36

*Astrometric-position errors caused by the tropospheric zenith delay error of 20 mm, the ionospheric TEC error of 10 TECU (8 mm at 22 GHz), the station position error of 3 mm, and the instrumental delay error of 0.1 mm (see text). RSS is the root-sum-square of five error sources.

(Honma et al. 2008a) are used for the delay calibration in VERA, to achieve a high astrometric precision. Their calibration errors are estimated to be 10–20 mm for the tropospheric zenith delay (Honma et al. 2008b; Nagayama et al. 2015), 3–10 TEC Unit (TECU) for the ionospheric TEC (Ho et al. 1997), 3 mm for the station position (Jike et al. 2009, 2018), and 0.1 mm for the instrumental delay between the dual-beam systems (Honma et al. 2008a). The ionosphere is dispersive, which means that the ionospheric delay depends on the observing frequency: a TEC error of 3–10 TECU is equivalent to 2–8 mm at the observing frequency of 22 GHz. The astrometric-position errors caused by these calibration errors for a single baseline and a single observation epoch are summarized in table 1. These values were theoretically estimated using the equations of Honma et al. (2010) at each separation and each elevation angle under VERA's maximum baseline length of 2300 km. The position error caused by the thermal noise was estimated using equation (1) in Reid et al. (1988) to be $\Delta\theta_{\text{th}} \approx 0.5 \cdot \theta_{\text{beam}}/\text{SNR} \approx 17 \mu\text{as}$ for a point source in the typical case of a synthesized beam size of $\theta_{\text{beam}} = 1 \text{ mas}$ and a signal-to-noise ratio (SNR) of the peak and rms flux density of the maser spot in the map of $\text{SNR} = 30$. A comparison of the estimated position errors indicates that the tropospheric contribution is dominant and strongly dependent on both the elevation and separation angles. Therefore, it is suggested that the parallax measurement at the 10 μas level is feasible for the close separation and high elevation sources (Honma et al. 2010).

In this study, we quantitatively investigate the effect of these error sources on the astrometric position error of the actual observations. We also evaluate the astrometric performance of VERA through the parallax measurements of five star-forming regions located at distances in the range of 5–11 kpc from the Sun.

¹ (<http://aiuws.unibe.ch/ionosphere/>).

Table 2. Source information.*

No	Source	α (J2000.0)	δ (J2000.0)	I_{peak} (Jy beam ⁻¹)	θ_{beam} (mas \times mas, $^{\circ}$)	θ_{SA} ($^{\circ}$)	θ_{PA} ($^{\circ}$)	$\Delta \text{sec } Z$
1	G135.28+02.80	02 ^h 43 ^m 28 ^s .5825	+62 $^{\circ}$ 57′08″.390	3–43	1.14 \times 0.80, –54	0.51	–19	0.0061
	J0244+6228	02 ^h 44 ^m 57 ^s .696681	+62 $^{\circ}$ 28′06″.51550	0.92–1.56	1.16 \times 0.84, –54			
2	G137.07+03.00	02 ^h 58 ^m 13 ^s .1793	+62 $^{\circ}$ 20′32″.915	4–16	1.18 \times 0.82, –49	1.05	–111	0.0204
	J0306+6243	03 ^h 06 ^m 42 ^s .659552	+62 $^{\circ}$ 43′02″.02414	0.10–0.22	1.18 \times 0.84, –49			
3	G200.08–01.63	06 ^h 21 ^m 47 ^s .5742	+10 $^{\circ}$ 39′22″.811	2–6	1.31 \times 0.82, –42	0.93	–105	0.0138
	J0625+1053	06 ^h 25 ^m 25 ^s .961188	+10 $^{\circ}$ 53′43″.88032	0.12–0.14	1.37 \times 0.83, –37			
4	G037.50+00.53	18 ^h 57 ^m 53 ^s .3876	+04 $^{\circ}$ 18′17″.394	7–11	1.51 \times 0.87, –40	1.08	–2	0.0205
	J1858+0313	18 ^h 58 ^m 02 ^s .352576	+03 $^{\circ}$ 13′16″.30172	0.14–0.28	1.52 \times 0.85, –47			
5	G037.82+00.41	18 ^h 58 ^m 53 ^s .8800	+04 $^{\circ}$ 32′15″.004	9–95	1.55 \times 0.86, –40	1.33	9	0.0228
	J1858+0313	18 ^h 58 ^m 02 ^s .352576	+03 $^{\circ}$ 13′16″.30172	0.14–0.28	1.52 \times 0.85, –47			

*Column 1: the source pair number. Column 2: the source name, where G and J denote the target and the reference source, respectively. Columns 3–4: the delay tracking center in the RA and Dec coordinates. Column 5: the peak intensity. Column 6: the synthesized beam size in major axis \times minor axis, and its position angle. Columns 7–8: the separation angle and the position angle between the target and the reference source, respectively. Column 9: the average $\Delta \text{sec } Z$ between the target and the reference source.

2 Observations

Astrometric observations of five H₂O maser sources at 22.235080 GHz frequency were conducted with VERA, consisting of four antennas with a 20 m dish located at Mizusawa (hereafter referred to as MIZ), Iriki (IRK), Ogasawara (OGA), and Ishigaki-jima (ISG). The observed target H₂O maser sources and the position reference continuum sources are listed in table 2. Hereafter, we refer to each target maser source by its first seven characters, namely, G135.28, G137.07, G200.08, G037.50, and G037.82. The target and its reference source were simultaneously observed using the dual-beam receiving system of VERA (Kawaguchi et al. 2000). The source coordinates, peak intensity, synthesized beam size, separation angle, position angle of the target with respect to its reference source, and the value of $\Delta \text{sec } Z$ are summarized in table 2, where $\Delta \text{sec } Z = |\text{sec } Z_{\text{tar}} - \text{sec } Z_{\text{ref}}|$ is the difference in sec Z between the target and reference sources described by the zenith angle Z ; this is an important parameter related to the astrometric position error caused by the tropospheric zenith delay error and is discussed in detail in sub-subsection 5.1.1. The values $\Delta \text{sec } Z$ are different at each station and changes with the hour angle by a factor of 2–3 during the observations. The average $\Delta \text{sec } Z$ of all stations during the observations has been calculated and is listed in table 2.

Table 3 lists the observation dates: A typical observation duration per epoch was 8 hr. We observed two maser sources together in the same epoch and we switched two maser sources every 10 min for G135.28 and G137.07, 30 min for G200.08 and G224.35–02.01, and 20 min for G037.50 and G037.82. The typical on-source time for each maser source was 3 hr. However, the maser of G224.35–02.01, whose coordinates are

Table 3. VERA observations.*

Source	Epoch	Obs. code	Date (yyyy mm dd)
G135.28 &	1	r07297a	2007 10 24
	2	r08007a	2008 01 08
G137.07	3	r08056a	2008 02 25
	4	r08160b	2008 06 08
	5	r08191a	2008 07 09
	6	r08218a	2008 08 05
	7	r08342a	2008 12 07
	8	r09044a	2009 02 13
	9	r09125b	2009 05 05
	10	r09251a	2009 09 08
G200.08	1	r16158a	2016 06 06
	2	r16330b	2016 11 25
	3	r16356a	2016 12 21
	4	r17030a	2017 01 30
	5	r17050a	2017 02 19
	6	r17076a	2017 03 17
	7	r17117a	2017 04 27
	8	r17159a	2017 06 08
	9	r17266c	2017 09 23
G037.50 &	1	r13019c	2013 01 19
	2	r13080b	2013 03 21
G037.82	3	r13153b	2013 06 02
	4	r13264a	2013 09 21
	5	r13358b	2013 12 24
	6	r14067b	2014 03 08
	7	r14133b	2014 05 13
	8	r14293a	2014 10 20

*Column 1: the source name. Column 2: the epoch number. Column 3: the observation code in VERA project. Column 4: the observation date.

$(\alpha, \delta)_{\text{J2000.0}} = (07^{\text{h}}05^{\text{m}}12^{\text{s}}.7, -11^{\circ}04′29″)$, could not be detected persistently for more than two epochs because of the maser time variation. Therefore, this source has been excluded from this paper. The fringe-finders 3C

84 for G135.28 and G137.07, OJ287 for G200.08, and J2015+3710 for G037.50 and G037.82, were observed every 80 min in order to calibrate the clock delay offset and rate. Left-band circular polarization signals were sampled with 2-bit quantization and filtered to $16 \text{ MHz} \times 16$ IF bands by the VERA digital filter unit (Iguchi et al. 2005). We assigned one IF band to the target maser source and the remaining 15 IF bands to the reference continuum source.

Correlation processing of the VERA observations was performed using the FX hardware correlator located at the National Astronomical Observatory of Japan (NAOJ) Mitaka campus until early 2015 (Shibata et al. 1998). Since 2015, regular operations of the newly developed software correlator has been started in the NAOJ Mizusawa campus (Oyama et al. 2016). Therefore, the observations of G135.28, G137.07, G037.50, and G037.82 before 2015 were processed using the Mitaka hardware correlator, while the observations of G200.08 after 2015 were processed using the Mizusawa software correlator. The visibility integration time of the correlation processing was 1 s. The velocity resolution was 0.42 km s^{-1} for G200.08 and 0.21 km s^{-1} for the other four maser sources.

The system noise temperature including atmospheric attenuation was measured using the chopper-wheel method (Ulich & Haas 1976) and monitored during the observations: its value under good weather conditions was 100–200 K and 200–300 K during the winter and summer seasons. The aperture efficiencies of the four antenna were 0.41–0.47 at the observing frequency of 22 GHz. Using a system noise temperature of $T_{\text{sys}} \approx 100\text{--}300 \text{ K}$ and an effective aperture area of $A_e = \pi r^2 \eta_a \approx 140 \text{ m}^2$ for the antenna dish radius of $r = 10 \text{ m}$ and an aperture efficiency of $\eta_a \approx 0.44$, the system equivalent flux density was calculated to be $\text{SEFD} = 2kT_{\text{sys}}/A_e \approx 2000\text{--}6000 \text{ Jy}$. The baseline-based noise level was 7–20 mJy at the fringe integration time of 1–2 min and a bandwidth of 240 MHz. The reference continuum sources could be detected on individual baselines with $\text{SNR} \geq 5$. The noise level of the phase-referenced image of the target maser spot was typically $0.1\text{--}0.3 \text{ Jy beam}^{-1}$. The maser spot whose peak intensity exceeds $1\text{--}2 \text{ Jy beam}^{-1}$ was detectable at the criterion of $\text{SNR} \geq 7$.

3 Calibration

Because the phase-referencing performance of VERA is evaluated in this paper, we summarize in this section the calibration method used for the phase-referencing analysis of VERA. An accurate delay calibration is required at $(\Delta\theta \cdot D)/(\epsilon \cdot \theta_{\text{SA}}) \approx 10 \text{ ps}$ level is required for the high-precision VLBI astrometry at the $\Delta\theta \approx 10 \text{ } \mu\text{as}$ level, under the conditions of the baseline length of $D \approx 2300 \text{ km}$ and the separation angle of $\theta_{\text{SA}} \approx 1^\circ$. Furthermore, because the a priori delay model used in the correlation processing is not

accurate enough for the high-precision VLBI astrometry, we recalculated the precise delay using the CALC3 software package developed for the Geodetic VLBI observations (Manabe et al. 1991; Jike et al. 2009) based on the following accurate geophysical models and data.

The geometric delay has been calculated using the Earth orientation parameter EOP 08 C04 (IAU1980; C. Bizouard & D. Gambis 2011),² produced by the International Earth Rotation and Reference System Service, and the station position measured by the Geodetic VLBI observations (Jike et al. 2009, 2018), and the source coordinates of both target maser and reference sources. For the reference sources, the coordinates listed in the VLBA calibrator source list were used.³ J0244+6228, J0306+6243, and J1858+0313 are second realizations of the International Celestial Reference Frame (ICRF2) sources and J0625+1053 was the additional source found by Petrov (2016). The error of the absolute position was $\approx 8 \text{ mas}$ for J1858+0313 and $\leq 1 \text{ mas}$ for the other reference sources. For the target maser source, we set the position of the maser spot used for the parallax measurement within 100 mas; these source coordinates are listed in table 2. In the case of the delay tracking and the phase-referencing imaging performed at the position offsets of $\leq 10 \text{ mas}$ for the reference source and $\leq 100 \text{ mas}$ for the target maser source, the propagating astrometric position error is expected to be $\leq 10 \text{ } \mu\text{as}$ for the source pair of $\theta_{\text{SA}} = 1^\circ$ (Reid & Honma 2014).

The troposphere delay is the sum of dry and wet components: $\tau_{\text{tro}} = M_{\text{dry}} \cdot \text{ZHD}/c + M_{\text{wet}} \cdot \text{ZWD}/c$. Here, M_{dry} and M_{wet} are the mapping functions for the dry and wet components, respectively. The Niell's mapping function (Niell 1996) was used in this paper. Values ZHD and ZWD are the zenith hydrostatic or dry delay (attributed to dry air) and the zenith wet delay (attributed to precipitable water vapor), respectively. The ZHDs of MIZ, IRK, OGA, and ISG were calculated to be 2.2715, 2.1534, 2.2298, and 2.2843 m, respectively, from the height of each station, h , using the formula: $\text{ZHD} = K_1 R/(gM_D) \cdot P_0 \cdot \exp(-h/h_0)$, where K_1 is the constant of Smith–Weintraub equation (Smith & Weintraub 1953), R is the universal gas constant, g is the gravitational acceleration, M_D is the molecular weight of the dry air in the troposphere, P_0 is the air pressure, and h_0 is the scale height of the dry air [equation (13.13) in Thompson et al. 2017]. The ZWD was obtained using $\text{ZWD} = \text{ZTD} - \text{ZHD}$ from the zenith total delay, ZTD, measured by the GPS (Honma et al. 2008b), using the GIPSY OASIS II 6.4 software package. The ZWD is obtained at 5 min intervals and fluctuates between 0.05 and 0.40 m.

² C. Bizouard & D. Gambis 2011 (https://hpiers.obspm.fr/iers/eop/eopc04_08/C04_guide.pdf).

³ (<http://www.vlba.nrao.edu/astro/calib>).

The ionosphere delay is calculated based on a single-layer model expressed as $\tau_{\text{ion}} = cr_e/(2\pi\nu^2) \cdot I_e \cdot \sec Z'$ with $\sin Z' = R/(R + H) \cdot \sin Z$, where r_e is the classical electron radius, I_e is the TEC, ν is the observed frequency, $\sec Z'$ is the mapping function of the ionosphere, $R \approx 6371$ km is the mean earth radius, $H = 450$ km is the height of the single-layer (ionosphere) above the Earth's mean surface, and Z is the zenith angle (Schaer 1999). The TEC is obtained at each station every 1 hr (2 hr before 2013) using CODE's GIM.¹

The instrumental delay difference between the dual-beam receivers was measured by the horn-on-dish method during the observations. In this method, the artificial wide-band radio noise is injected from the noise sources mounted on the antenna feedome base into the dual-beam receivers after reflection by a sub-reflector (Honma et al. 2008a). The delay difference between the dual-beam receivers and its time variation can be simultaneously monitored by monitoring the correlation of the common noise source signal between the dual-beam receivers.

These calculated and measured delays were formatted into the Astronomical Image Processing System (AIPS) SN table format and applied to the visibility data. The amplitude calibration, bandpass calibration, fringe search, self-calibration, and image synthesis were performed using AIPS. The amplitude calibrations were performed based on the gain curve and system noise temperatures using APCAL. The bandpass calibration was performed to utilize the autocorrelation spectrum of the fringe finder sources using BPASS. The fringe search of the reference source was performed by 1 or 2 min integration and a 0.5 min interval using FRING. The self-calibration image of the reference source was obtained to solve their structure effects using IMAGR and CALIB. The delay and phase solutions of the fringe search and the self-calibration were applied to the target maser sources using TACOP together with the dual-beam delay calibration and the delay tracking recalculation SN tables using TBIN. Next, the calibrated visibility of the target maser was Fourier transformed to synthesize images by IMAGR. Each velocity channel was imaged on a field of $8'' \times 8''$ with 8192×8192 grid around the delay tracking center, and the brightness peak was searched. For each peak, the phase-referencing image of $100 \text{ mas} \times 100 \text{ mas}$ with 2048×2048 grid was obtained using the CLEAN process, and the peak position, peak intensity, and rms noise level were obtained using the two-dimensional Gaussian fitting by IMFIT.

4 Results

The parallaxes of the five star-forming regions were measured to be 0.089–0.200 mas, corresponding to the distances of 5–11 kpc at 10%–20% uncertainties. Figure 1

shows the sinusoidal apparent motion caused by the parallax with a one-year period, after removing the individual position offset origins and the proper motions. The amplitude corresponds to the parallax. The position of the maser spot at each observing epoch was measured to fit the maser emission on the phase-referencing image by the single Gaussian component, and its positional variation was monitored for 1–2 years.

Figure 2 shows the phase-referencing images of the representative maser spots used for the parallax measurement. Their spatial structures were basically compact and point-like. The compact maser spots, which have been persistent for more than one year, were selected for the parallax measurements: a single maser spot for G135.28, and two or three maser spots for the other four sources. We fitted the measured positions with five parameters of the position offset origin, $(\Delta\alpha\cos\delta, \Delta\delta)$, the linear proper motion, $(\mu_\alpha\cos\delta, \mu_\delta)$, and the parallax, π , by the least-squares method. Table 4 summarizes the five obtained parameters and the standard deviation of the post-fit residual. The obtained parallaxes of the individual maser spots for the four sources with multiple spots are consistent with each other. Hence, we conducted the combined fitting, in which the positions of the spots were simultaneously fitted with one common parallax, while allowing for different proper motions and position offsets for individual spots.

As discussed in previous studies on VLBI astrometry (Hachisuka et al. 2006; Honma et al. 2007), the standard deviation of the post-fit residual (σ_{res}) of the least-squares fitting, which results in a reduced chi-square of unity ($\chi^2_\nu \approx 1$), is regarded as the astrometric position error of the measurement with one observing epoch. Then, the parallax error is calculated using the covariance matrix, which can be approximately expressed as $\sigma_\pi \approx \sigma_{\text{res}}/\sqrt{N_d}$, using the post-fit residual of σ_{res} and the number of the data, $N_d = N_{\text{obs}} \times N_{\text{spot}}$. Here, N_{obs} and N_{spot} are the number of observations and maser spots, respectively. Random-like errors such as the maser spot structure variation could not be correlated with each other between different spots, whereas systematic errors such as the tropospheric zenith delay error have a similar effect on all maser spots. Because the post-fit residuals of different spots show similar values, we considered that the systematic error would be dominated. Therefore, the parallax error of the combined fitting was multiplied by a factor of $\sqrt{N_{\text{spot}}}$, i.e., it was expressed as $\sigma_\pi \approx \sigma_{\text{res}}/\sqrt{N_{\text{obs}}}$. As shown in table 4, the post-fit residuals of the five target sources are estimated to be approximately 30–60 μas . Because the observations of 8–10 epochs can statistically reduce the parallax error compared with the post-fit residual by a factor of approximately 1/3, the parallax errors are estimated to be

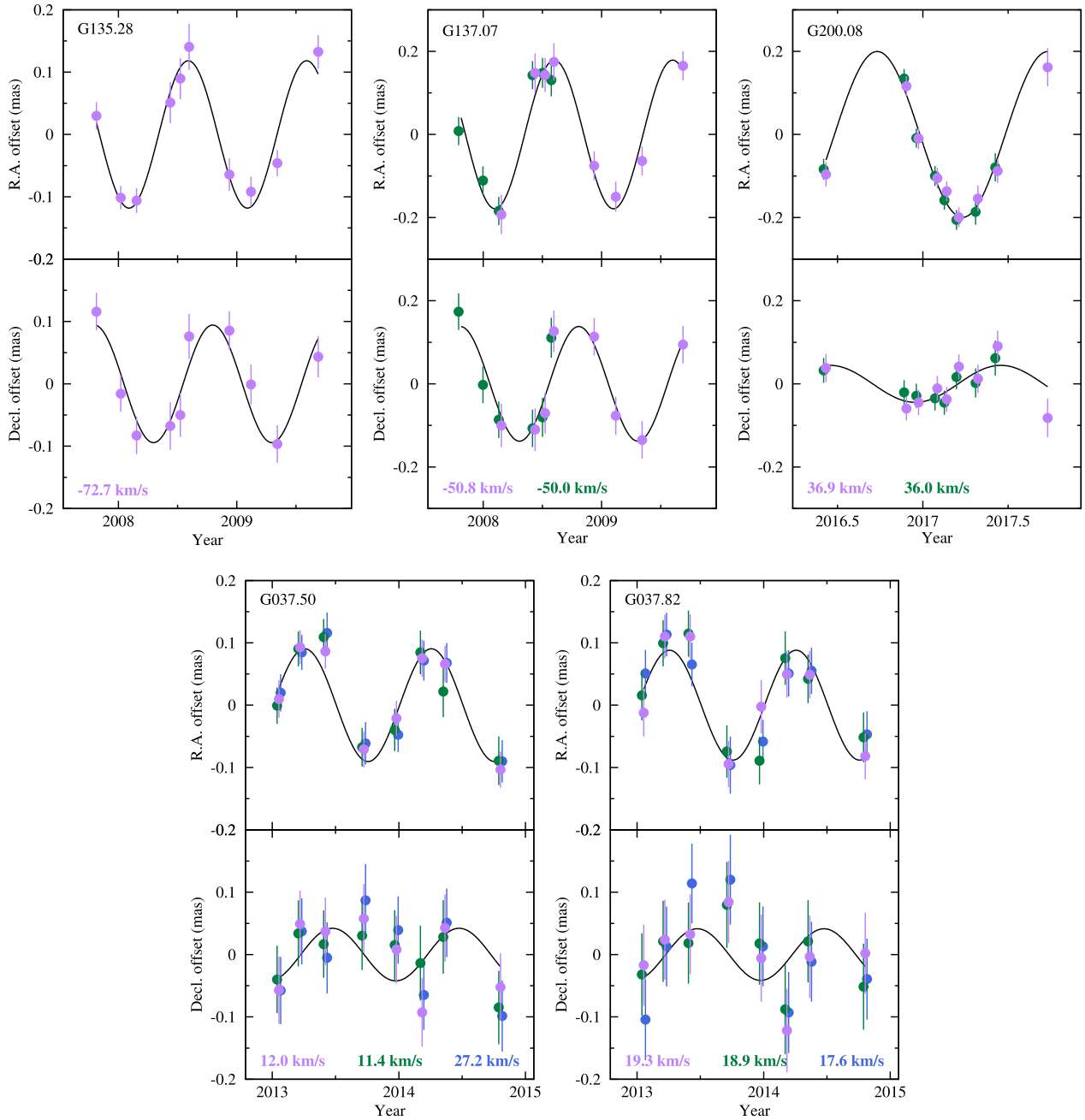


Fig. 1. Parallaxes of G135.28, G137.07, G200.08, G037.50, and G037.82. Individual proper motions and position offsets are removed to better show the parallax signatures. The data for the different maser spots shown in each color are slightly shifted in time for clarity. (Color online)

approximately $10\text{--}20\ \mu\text{s}$. When comparing the parallax errors in table 4, it should be noted the difference in the number of detection. The number of detection varies from 5 to 10 epochs for each spot. This is expected to affect the difference in the parallax errors by a factor of $\sqrt{(10/5)} = 1.4$.

The astrometric position error caused by the thermal noise was estimated to be $\Delta\theta_{\text{the}} = 14\text{--}20\ \mu\text{s}$ for each target source by the 2D Gaussian fitting to the maser spot emission

on the phase-referencing image using AIPS IMFIT. This is equal to

$$\Delta\theta_{\text{the}} \approx 0.5 \cdot \frac{\theta_{\text{beam}}}{\text{SNR}} \quad (1)$$

for the point source (Reid et al. 1988), where θ_{beam} is the synthesized beam size and SNR is the signal-to-noise ratio of the maser emission on the phase-referencing image. The

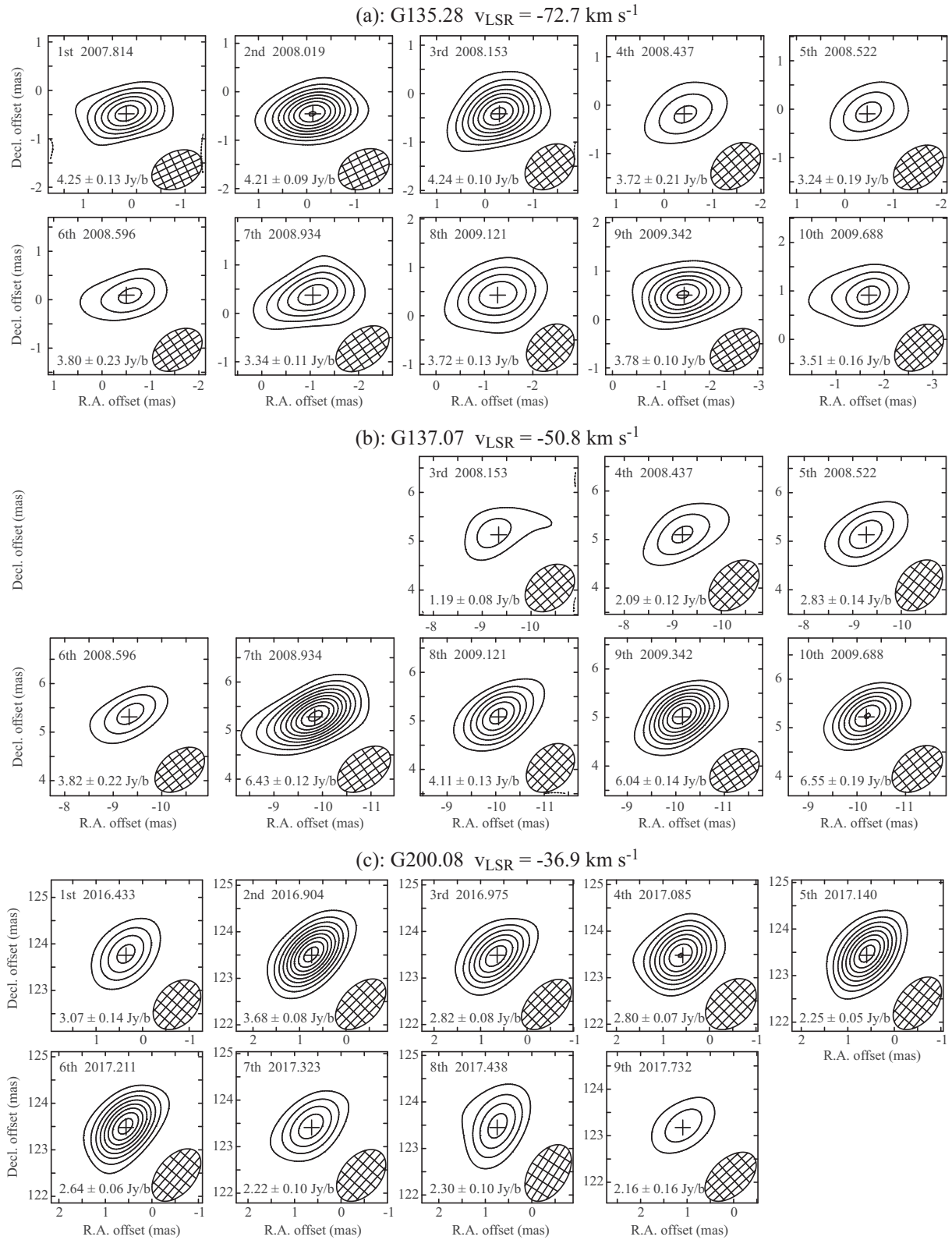


Fig. 2. Phase-referencing images of the maser spots in (a) G135.28, (b) G137.07, (c) G200.08, (d) G037.50, and (e) G037.82. The observation number and the observation date in years are shown in the top left-hand corner of each panel. The peak intensity (I_{peak}) and the rms noise level (σ) are shown by $I_{\text{peak}} \pm \sigma \text{ Jy beam}^{-1}$ in the bottom left-hand corner. The contour levels are 5σ , 10σ , 15σ , 20σ , The synthesized beam is shown in the bottom right-hand corner.

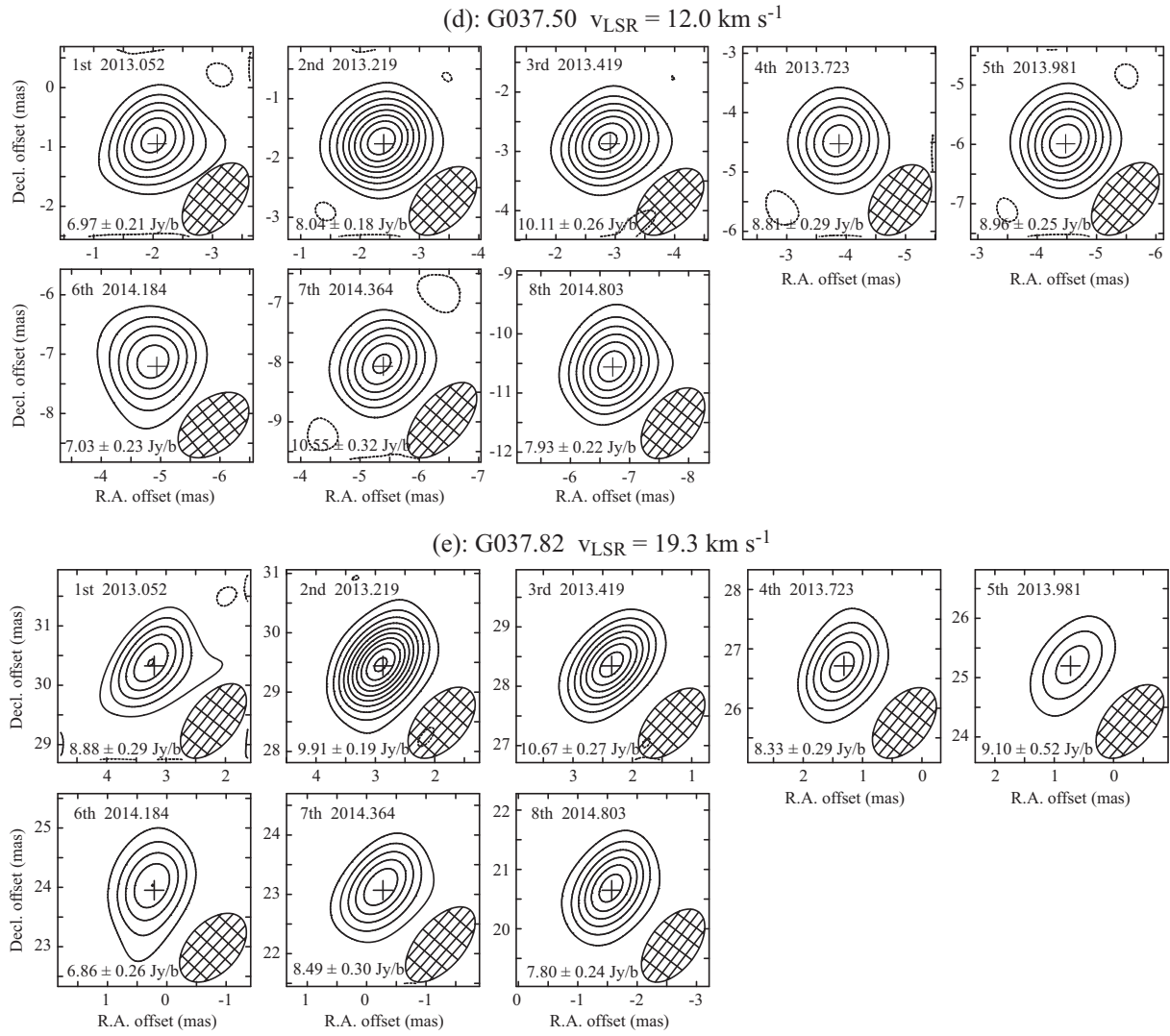


Fig. 2. (Continued)

estimated errors of the five sources are consistent with $\Delta\theta_{\text{the}} \approx 17 \mu\text{as}$, which is calculated in the typical case of $\theta_{\text{beam}} = 1 \text{ mas}$ and $\text{SNR} = 30$. Because all spots used in the parallax fitting were detected at $\text{SNR} \geq 13$, the position errors of the thermal noise were less than $38 \mu\text{as}$ under any observation and in any spot. The value of $\Delta\theta_{\text{the}}$ in table 5 is the average of all observations and spots.

The uncalibrated delay errors of the troposphere, ionosphere, station position, and instrument are significant error sources of the VLBI astrometry, which cause the common position offset between the different maser spots and sources. For example, in G037.50 and G037.82, it appears to be a position offset of $\sim 50 \mu\text{as}$ in the Dec direction (see figure 1). Because these two sources were observed in the same observation, the uncalibrated delay errors commonly affect and cause the similar position

offset. The post-fit residual is larger than the position error caused by the thermal noise, and the χ^2_{ν} value of the parallax-fitting is much larger than 1, if only the thermal noise error is considered. These mean that the position error of the thermal noise underestimates the true position error. Therefore, the error floor, $\Delta\theta_{\text{flo}}$ (Reid et al. 2009), is estimated to add in quadrature to the position error of the thermal noise until we achieved $\chi^2_{\nu} \approx 1$, i.e., $\sigma_{\text{res}} = \sqrt{(\Delta\theta_{\text{the}}^2 + \Delta\theta_{\text{flo}}^2)}$. As summarized in table 5, the estimated error floors of individual target sources are in the range of $\Delta\theta_{\text{flo}} \approx 20\text{--}60 \mu\text{as}$ and vary between the target sources by a factor of 3. Furthermore, this difference appears to be related to the separation angles between the target and reference sources. The error floor represents the systematic error from the uncalibrated delay contributions of the troposphere, ionosphere, station position, and

Table 4. Parallax and proper motion fitting.*

Source	v_{LSR} (km s^{-1})	π (mas)	$\mu_{\alpha} \cos \delta$ (mas yr^{-1})	μ_{δ} (mas yr^{-1})	$\Delta \alpha \cos \delta$ (mas)	$\Delta \delta$ (mas)	$\sigma_{\text{res}, \alpha}$ (mas)	$\sigma_{\text{res}, \delta}$ (mas)
G135.28	−72.7	0.124 ± 0.011	-1.05 ± 0.01	0.78 ± 0.02	0.20 ± 0.01	-0.58 ± 0.02	0.026	0.033
G137.07	−50.8	0.191 ± 0.016	-0.81 ± 0.03	-0.06 ± 0.03	-9.12 ± 0.03	5.24 ± 0.03	0.036	0.043
	−50.0	0.179 ± 0.029	-0.46 ± 0.08	0.11 ± 0.09	0.09 ± 0.04	0.04 ± 0.04	0.043	0.055
	Combined	0.187 ± 0.016					0.040	0.048
G200.08	36.0	0.210 ± 0.019	0.18 ± 0.04	0.05 ± 0.03	-0.67 ± 0.02	-0.35 ± 0.02	0.024	0.023
	36.9	0.190 ± 0.015	0.39 ± 0.03	-0.35 ± 0.04	0.39 ± 0.03	123.74 ± 0.03	0.026	0.039
	Combined	0.200 ± 0.017					0.027	0.033
G037.50	11.4	0.084 ± 0.018	-2.85 ± 0.03	-5.62 ± 0.03	-251.84 ± 0.02	-134.60 ± 0.02	0.036	0.041
	12.0	0.095 ± 0.011	-2.60 ± 0.01	-5.50 ± 0.03	-2.05 ± 0.01	-0.85 ± 0.03	0.021	0.053
	27.2	0.089 ± 0.018	-2.81 ± 0.02	-5.56 ± 0.04	-248.63 ± 0.02	-136.06 ± 0.04	0.033	0.068
	Combined	0.091 ± 0.016					0.031	0.055
G037.82	17.6	0.087 ± 0.018	-2.75 ± 0.02	-5.05 ± 0.05	3.59 ± 0.02	82.58 ± 0.05	0.032	0.078
	18.9	0.083 ± 0.023	-3.10 ± 0.03	-5.54 ± 0.04	-3.10 ± 0.03	18.31 ± 0.03	0.046	0.054
	19.3	0.090 ± 0.019	-2.70 ± 0.03	-5.54 ± 0.04	3.24 ± 0.02	30.36 ± 0.04	0.036	0.062
	Combined	0.089 ± 0.020					0.038	0.066

*Column 1: the source name. Column 2: the LSR velocity of the maser spot. “Combined” means the combined fitting (see section 4). Column 3: the parallax. Columns 4–5: the proper motions in RA and Dec, respectively. Columns 6–7: the position offsets in RA and Dec, respectively, with respect to the delay tracking center in table 1. Columns 8–9: the standard deviations of the post-fit residuals in RA and Dec, respectively.

Table 5. Observational estimation of the astrometric position errors using the post-fit residual of the parallax fitting.*

Source	σ_{res} (μas)		$\Delta\theta_{\text{the}}$ (μas)		$\Delta\theta_{\text{flo}}$ (μas)	
	α	δ	α	δ	α	δ
G135.28	26	33	20	16	16	28
G137.07	40	48	17	14	33	44
G200.08	27	33	16	17	21	27
G037.50	31	55	18	18	25	52
G037.82	38	66	17	19	34	63

*Column 1: the source name. Columns 2–3: the standard deviation of the post-fit residuals (σ_{res}) in table 4, $v_{\text{LSR}} = -72.7 \text{ km s}^{-1}$ for G135.28 and the combined fitting for the other four sources. Columns 4–5: the position errors caused by the thermal noise ($\Delta\theta_{\text{the}}$). Columns 6–7: the error floor estimated by $\Delta\theta_{\text{flo}} = \sqrt{(\sigma_{\text{res}}^2 - \Delta\theta_{\text{the}}^2)}$.

instrument. Therefore, we estimated the error floor for a direct comparison between measurements regardless of the thermal noise contribution. The error floor has been discussed in detail in subsection 5.2.

The weather condition is also expected to have a significant effect on the astrometric position error. For instance, bad weather conditions in summer compared to winter increases the system noise temperature and the tropospheric zenith delay by a factor of 2–3. We investigated the effect of such weather conditions on the astrometric position error, using the post-fit residuals of the parallax fitting of the five sources. For this, we divided the year into summer

(April to September) and winter (October to March) seasons and derived the standard deviations of their post-fit residuals to be 41 and 32 μas , respectively, indicating a slight increase in the astrometric position error by a factor of $41/32 = 1.3$.

The absolute proper motion of the maser spot, which was persistent for at least two observations, was obtained by the fitting of the linear motion and the position offset origin. Then, the parallax was fixed at the value shown in table 5. The distributions of the detected maser spots are shown in figure 3. The maser spots are distributed on a scale of $\sim 0''.1$. The average proper motion of all detected maser spots is summarized in table 6. The error of the average proper motion is the standard error (SE) calculated using $\text{SE} = \sigma_{\mu} / \sqrt{N_{\text{spot}}}$, where σ_{μ} is the standard deviation of the proper motion. The residual vector obtained by subtracting the average from the proper motion of each spot indicates the internal motion of each spot, which is also shown in figure 3. The internal motion velocities are approximately 5–30 km s^{-1} for each source. The average local standard of rest (LSR) velocity and its standard error are also calculated and summarized in table 6, which is consistent within 2 km s^{-1} with the LSR velocity observed in the molecular line of −72, −52, 34, 10, and 18 km s^{-1} for G135.28, G137.07, G200.08, G037.50, and G037.82, respectively (Wouterloot & Brand 1989; Bronfman et al. 1996). This indicates that the proper motion, as well as the LSR velocity, can be used to trace the systemic motion of the molecular gas.

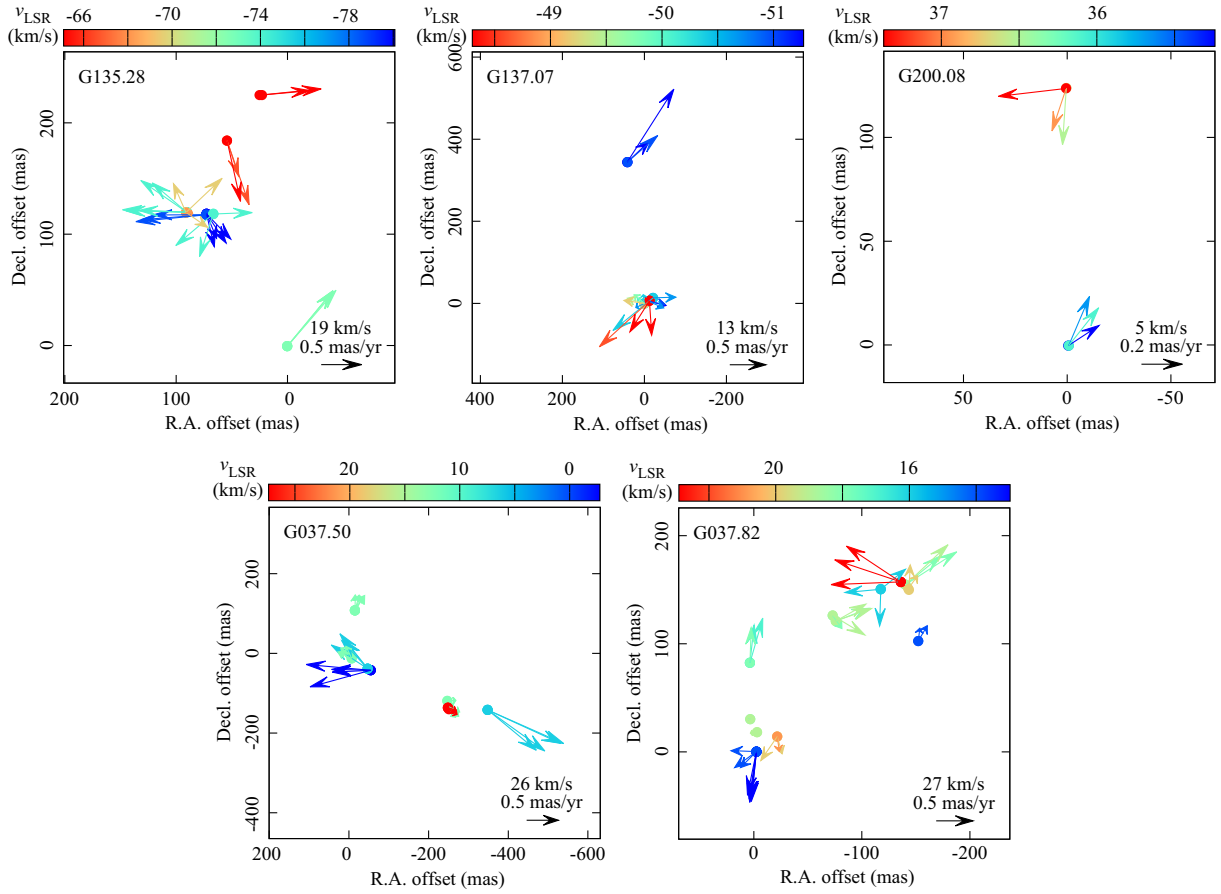


Fig. 3. Maser spot map with the internal motion vector of G135.28, G137.07, G200.08, G037.50, and G037.82. The color shows the LSR velocity. The map origin is the coordinate listed in table 2. The average internal motion velocity in units of mas yr⁻¹ and km s⁻¹ is shown by the black arrow in the bottom right-hand corner of each panel. (Color online)

Table 6. Parallax, distance, proper motion, and LSR velocity.*

Source	π (mas)	D (kpc)	$\bar{\mu}_\alpha \cos \delta$ (mas yr ⁻¹)	$\bar{\mu}_\delta$ (mas yr ⁻¹)	\bar{v}_{LSR} (km s ⁻¹)
G135.28	0.124 ± 0.011	$8.1^{+0.8}_{-0.7}$	-0.45 ± 0.20	0.09 ± 0.16	-72.9 ± 1.6
G137.07	0.187 ± 0.016	$5.4^{+0.5}_{-0.4}$	-0.57 ± 0.16	-0.01 ± 0.16	-50.1 ± 0.4
G200.08	0.200 ± 0.017	$5.0^{+0.5}_{-0.4}$	0.32 ± 0.14	-0.14 ± 0.16	36.3 ± 0.6
G037.50	0.091 ± 0.016	$11.0^{+2.3}_{-1.6}$	-2.74 ± 0.18	-5.49 ± 0.10	10.7 ± 2.6
G037.82	0.089 ± 0.020	$11.2^{+3.3}_{-2.1}$	-2.73 ± 0.12	-5.53 ± 0.12	17.5 ± 0.8

*Column 1: the source name. Column 2: the parallax obtained by the combined fitting. Column 3: the source distance from the Sun. Columns 4 and 5: the average proper motions of H₂O masers in RA and Dec, respectively. Column 6: the average LSR velocity of H₂O masers.

5 Discussion

5.1 Error estimation in calibration

We estimated the post-fit residual, which is regarded as the true position error in the VLBI astrometry, and found that most of it originates in uncalibrated delay errors of the troposphere, ionosphere, station position, and instrument. We next attempted to identify the major source among them. For this, we quantitatively estimated the position errors caused by the troposphere ($\Delta\theta_{\text{tro}}$), ionosphere ($\Delta\theta_{\text{ion}}$),

station position ($\Delta\theta_{\text{sta}}$), and instrument ($\Delta\theta_{\text{ins}}$) under the actual observational conditions. The simple theoretical estimation under the single baseline has already been mentioned in section 1. However, in the actual observations, the elevation angle, the hour angle, and the UV distance change during the observations, and are also different in each station and each baseline. Therefore, to estimate a more realistic error under the actual observational conditions, we performed an artificial offset analysis (Nagayama et al. 2015), wherein an artificial delay offset was added to

the observed visibility data and the positional change of the maser spot was measured on the phase-referencing map. Then, we obtained the error sensitivity of the effect of the delay error on the position error. We performed this analysis on four error sources and five target sources. We used the visibility data of the seventh epoch for G135.28 and G137.07, the fifth epoch for G200.08, and the second epoch for G037.50 and G037.82. The results of individual error sources are described in sub-subsections 5.1.1 to 5.1.4.

5.1.1 Troposphere

While the short-term tropospheric fluctuation can be calibrated by phase-referencing (i.e., applying the phase solution obtained by the reference source to the target source), the long-term tropospheric delay difference between the two sources still remains because of their separation on the sky. This term is calibrated using the tropospheric zenith delay and the tropospheric mapping function (see section 3). The tropospheric zenith delay error is estimated to be 10–20 mm from the comparisons of several estimations from the GPS data, geodetic VLBI data, image-optimization data, and grid meteorological data (Honma et al. 2008b; Nagayama et al. 2015).

We investigate the propagation of tropospheric zenith delay error ($c\Delta\tau_{\text{tro}}$) to the astrometric-position error ($\Delta\theta_{\text{tro}}$). The artificial offset ranging from -60 to $+60$ mm with a step of 20 mm was constantly added to the tropospheric zenith delay of each station throughout the observation duration of 8 hr (no time variation). Then, the positional changes were obtained from the phase-referencing maps. The offset range was set at a value that is approximately 10 times larger than the actual tropospheric zenith delay error to obtain the exact position error sensitivity. This trial was made for each station and target source. The obtained positional changes are shown in figure 4a. The position appears to linearly vary with the tropospheric zenith delay offset. The slope in figure 4a was used to obtain the position error sensitivity of the troposphere, $\Delta\theta_{\text{tro}}/(c\Delta\tau_{\text{tro}})$, as shown in table 7. The obtained position error sensitivity of each station is consistent with the theoretical one estimated using $\Delta\theta_{\text{tro}}/(c\Delta\tau_{\text{tro}}) \approx \Delta \sec Z/D$ from the averaged $\Delta \sec Z$ and the averaged baseline length D for the observational duration. A detailed comparison between the artificial offset analysis and the theoretical estimation has been reported in Nagayama et al. (2015). Using the position error sensitivity and adopting the tropospheric zenith delay error of $c\Delta\tau_{\text{tro}} = 10$ mm for each station (Nagayama et al. 2015), the position error of the troposphere, $\Delta\theta_{\text{tro}}$, was obtained as shown in table 7. The total error for an array was estimated to combine the errors for each station by the

root-sum-square (RSS). Table 8 summarizes the experimentally estimated astrometric-position error for the array using the artificial offset analysis.

The relation between the position error and the tropospheric zenith delay error is theoretically given by the following expression:

$$\Delta\theta_{\text{tro}} \approx \frac{c\Delta\tau_{\text{tro}}}{D} \cdot \Delta \sec Z. \quad (2)$$

This equation is re-written as $\Delta\theta_{\text{tro}} \approx c\Delta\tau_{\text{tro}}/\lambda \cdot \Delta \sec Z \cdot \theta_{\text{beam}}$, using the relation between the beam size, wavelength, and the baseline length of $\theta_{\text{beam}} \approx \lambda/D$. Therefore, the position error should be proportional to $\Delta \sec Z$ and θ_{beam} . The estimated position error in table 8 shows that the smallest position error is $\sqrt{(\Delta\theta_{\text{tro},\alpha} \cdot \Delta\theta_{\text{tro},\delta})} = 8 \mu\text{as}$ for G135.28, which is the source with the smallest $\Delta \sec Z \approx 0.006$ and the smallest $\theta_{\text{beam}} \approx 1$ mas. Similarly, the largest one is $48 \mu\text{as}$ for G037.82, which is the source with the largest $\Delta \sec Z \approx 0.023$ and the largest $\theta_{\text{beam}} \approx 1.5$ mas. The $\Delta\theta_{\text{tro}}$ value of the two sources varies by a factor of $(48 \mu\text{as})/(8 \mu\text{as}) \approx 6$, which is due to the variation in the $\Delta \sec Z$ value by a factor of $0.023/0.006 \approx 4$ and the θ_{beam} value by a factor of $(1.5 \text{ mas})/(1 \text{ mas}) \approx 1.5$. The $\Delta \sec Z$ and θ_{beam} values for each source are shown in table 2. The error distribution in the RA and Dec directions is affected by the position angle of the source pair. The position error in RA is larger for the east–west pairs of G137.07 and G200.08, while that in Dec is larger for the north–south pairs of G135.28, G037.50, and G037.82.

5.1.2 Ionosphere

The position error sensitivity of the ionosphere was obtained using the same method as that of troposphere to add the artificial offset ranging from -90 to $+90$ TECU with a step of 30 TECU in the TEC. The obtained sensitivity and the position error of the ionosphere are shown in figure 4b, table 7, and table 8. The error of TEC is expected to be 3–10 TECU (Ho et al. 1997). We conservatively take 10 TECU for each station. The position error caused by the ionosphere was estimated to be $1\text{--}8 \mu\text{as}$ for each source, which has little effect on our observations at the frequency $\nu = 22$ GHz, because its effect is reduced by ν^{-2} . Based on the equation using the ionospheric calibration mentioned in section 3, the position error is expressed as follows:

$$\Delta\theta_{\text{ion}} \approx \frac{c\Delta\tau_{\text{ion}}}{D} \cdot \Delta \sec Z' = \frac{cr_e\Delta I_e}{2\pi\nu^2 D} \cdot \Delta \sec Z'. \quad (3)$$

The relationship between the position error and the separation and position angles of the source pair is basically similar to that of the troposphere, although there is a difference between the mapping functions of the ionosphere ($\sec Z'$) and the troposphere ($\sec Z$).

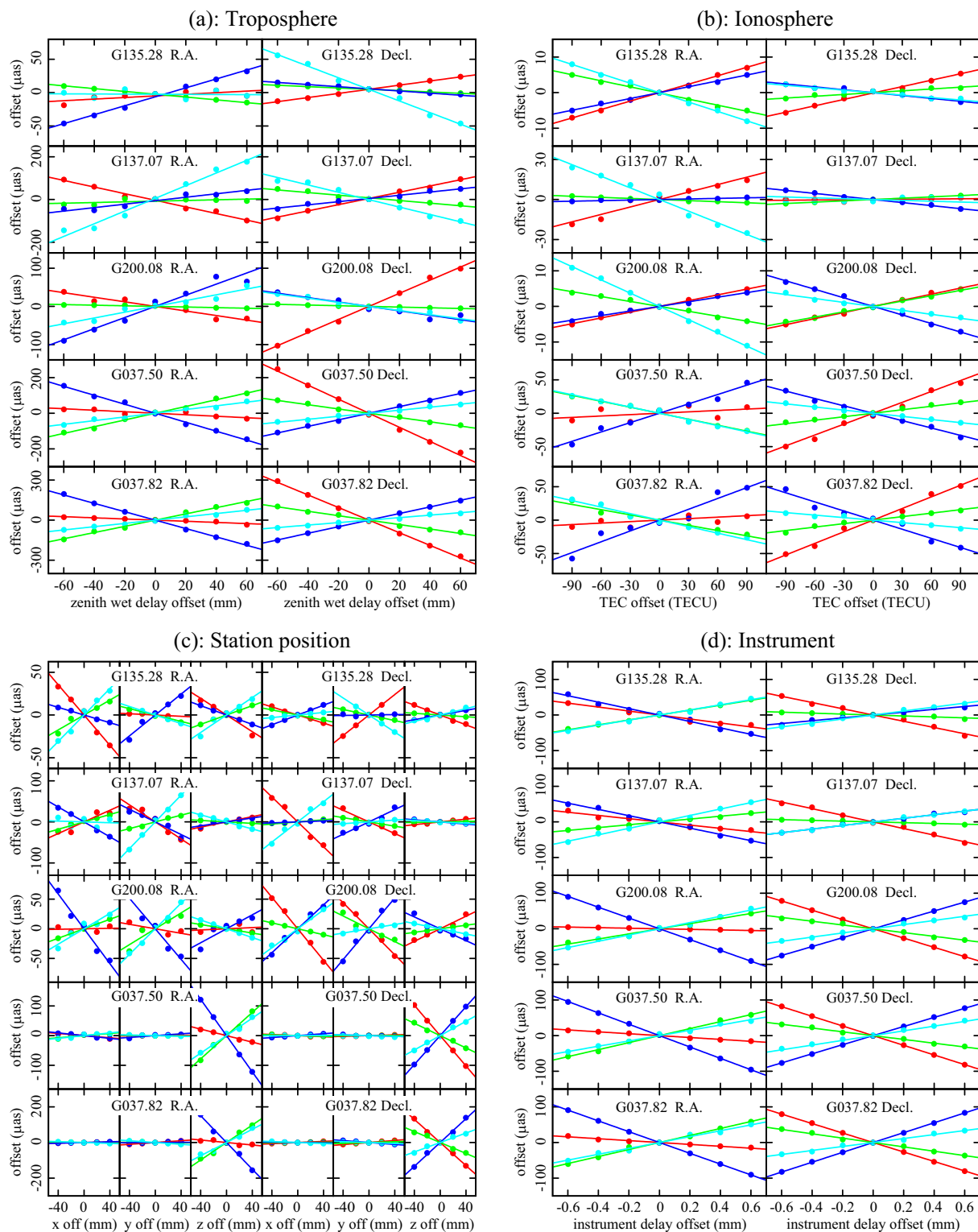


Fig. 4. Position error sensitivities of the (a) troposphere, (b) ionosphere, (c) station position, and (d) instrument obtained using the artificial offset analysis. The data of G135.28, G137.07, G200.08, G037.50, and G037.82 are shown from top to bottom. Left- and right-hand panels show the RA and Dec offsets, respectively. Red, green, blue, and cyan show MIZ, IRK, OGA, and ISG stations, respectively. The solid line shows the linear fitting. (Color online)

Table 7. Results of the artificial offset analysis.*

Sta.	Troposphere				Ionosphere				Station position				Instrument			
	$\Delta\theta/(c\Delta\tau)$ ($\mu\text{as mm}^{-1}$)		$\Delta\theta$ (μas)		$\Delta\theta/(c\Delta\tau)$ ($\mu\text{as TECU}^{-1}$)		$\Delta\theta$ (μas)		$\Delta\theta/(c\Delta\tau)$ ($\mu\text{as mm}^{-1}$)		$\Delta\theta$ (μas)		$\Delta\theta/(c\Delta\tau)$ ($\mu\text{as mm}^{-1}$)		$\Delta\theta$ (μas)	
	α	δ	α	δ	α	δ	α	δ	α	δ	α	δ	α	δ	α	δ
G135.28																
MIZ	0.12	0.31	1.2	3.1	−0.08	0.06	0.8	0.6	0.81	0.57	2.4	1.7	−56	−88	5.6	8.8
IRK	−0.21	−0.10	2.1	1.0	−0.06	0.02	0.6	0.2	0.44	0.18	1.3	0.5	69	−13	6.9	1.3
OGA	0.67	−0.16	6.7	1.6	0.06	−0.03	0.6	0.3	0.57	0.26	1.7	0.8	−90	40	9.0	4.0
ISG	−0.01	−0.87	0.1	8.7	−0.09	−0.02	0.9	0.2	0.77	0.43	2.3	1.3	72	56	7.2	5.6
RSS	0.71	0.94	7.1	9.4	0.14	0.07	1.4	0.7	1.33	0.78	4.0	2.3	146	112	14.6	11.2
G137.07																
MIZ	−1.55	1.46	15.5	14.6	0.19	0.01	1.9	0.1	1.30	1.69	3.9	5.1	−45	−93	4.5	9.3
IRK	0.16	−0.62	1.6	6.2	−0.03	0.03	0.3	0.3	0.62	0.29	1.8	0.9	40	−11	4.0	1.1
OGA	0.81	0.75	8.1	7.5	0.01	−0.08	0.1	0.8	1.22	0.76	3.6	2.3	−88	51	8.8	5.1
ISG	2.97	−1.73	29.7	17.3	−0.29	−0.02	2.9	0.2	1.69	1.24	5.1	3.7	90	51	9.0	5.1
RSS	3.45	2.46	34.5	24.6	0.35	0.09	3.5	0.9	2.53	2.25	7.6	6.7	140	118	14.0	11.8
G200.08																
MIZ	−0.60	1.72	6.0	17.2	0.05	0.06	0.5	0.6	0.20	1.81	0.6	5.4	−8	−130	0.8	13.0
IRK	−0.08	−0.09	0.8	0.9	−0.05	0.05	0.5	0.5	0.80	0.61	2.4	1.8	72	−53	7.2	5.3
OGA	1.46	−0.58	14.6	5.8	0.04	−0.08	0.4	0.8	2.04	1.72	6.1	5.2	−152	125	15.2	12.5
ISG	0.76	−0.54	7.6	5.4	−0.12	−0.04	1.2	0.4	1.31	0.85	3.9	2.5	88	59	8.8	5.9
RSS	1.75	1.90	17.5	19.0	0.14	0.12	1.4	1.2	2.56	2.71	7.7	8.1	190	197	19.0	19.7
G037.50																
MIZ	−0.42	−3.95	4.2	39.5	0.07	0.54	0.7	5.4	0.58	2.56	1.7	7.7	−27	−136	2.7	13.6
IRK	1.89	−1.20	18.9	12.0	−0.30	0.17	3.0	1.7	1.97	1.04	5.9	3.1	98	−53	9.8	5.3
OGA	−2.52	1.85	25.2	18.5	0.47	−0.37	4.7	3.7	3.07	2.45	9.2	7.3	−160	128	16.0	12.8
ISG	1.04	0.85	10.4	8.5	−0.31	−0.16	3.1	1.6	1.50	1.21	4.5	3.6	75	67	7.5	6.7
RSS	3.34	4.60	33.4	46.0	0.64	0.70	6.4	7.0	3.99	3.89	12.0	11.7	204	205	20.4	20.5
G037.82																
MIZ	−0.43	−4.72	4.3	47.2	0.07	0.58	0.7	5.8	0.43	3.27	1.3	9.8	−27	−133	2.7	13.3
IRK	2.33	−1.66	23.3	16.6	−0.26	0.17	2.6	1.7	2.46	1.54	7.4	4.6	98	−61	9.8	6.1
OGA	−3.14	2.47	31.4	24.7	0.54	−0.46	5.4	4.6	3.76	3.36	11.3	10.1	−152	138	15.2	13.8
ISG	1.23	0.93	12.3	9.3	−0.33	−0.13	3.3	1.3	1.88	1.34	5.6	4.0	83	56	8.3	5.6
RSS	4.12	5.66	41.2	56.6	0.69	0.77	6.9	7.7	4.89	5.11	14.7	15.3	200	209	20.0	20.9

*Column 1: the station name. RSS means the root-sum-square of four stations. Columns 2–5: the positional error sensitivity [$\Delta\theta/(c\Delta\tau)$] and the positional error ($\Delta\theta$) in RA (α) and Dec (δ) of the troposphere, respectively. Columns 6–9: those of the ionosphere. Columns 10–13: those of the station position. Columns 14–17: those of the instrument. The calibration error of each station is 10 mm for the tropospheric zenith delay, 10 TECU (8 mm at 22 GHz) for the ionospheric TEC, 3 mm for the station position, and 0.1 mm for the dual-beam instrumental delay.

5.1.3 Station position

In VERA, the station position is measured by the monthly geodetic observation and its error is estimated to be $c\Delta\tau_{\text{sta}} = 3$ mm (Jike et al. 2018). The artificial offset ranging from -40 to $+40$ mm with a step of 20 mm was added to the station position of (x, y, z) in the geocentric coordinates. The results of the artificial-offset analysis are shown in figure 4c, table 7, and table 8. The astrometric-position error caused by the station position error was estimated to be $3\text{--}15 \mu\text{as}$ for each source. It depends on the separation angle between the target and the reference sources, as can be seen from the following expression:

$$\Delta\theta_{\text{sta}} \approx \frac{c\Delta\tau_{\text{sta}}}{D} \cdot \theta_{\text{SA}}. \quad (4)$$

5.1.4 Instrument

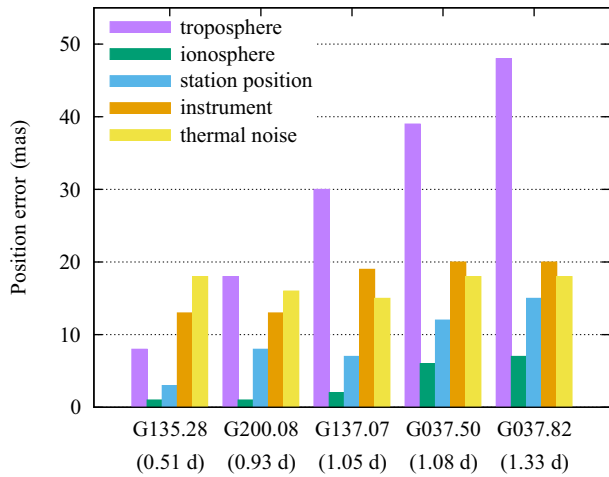
While the dual-beam receiving system of the VERA works well for reducing phase fluctuations caused by the troposphere (Honma et al. 2003), the use of two independent receivers causes an instrumental delay difference between the dual beams. This difference is calibrated by injecting the common noise source signal into the dual-beam receivers and monitoring the correlation between the dual beams during the observations. This calibration error is estimated to be $c\Delta\tau_{\text{ins}} \sim 0.1$ mm (Honma et al. 2008a).

The artificial offset ranging from -0.6 to $+0.6$ mm with a step of 0.2 mm was added to the calibration data of the instrumental delay difference, and its error sensitivity and position error were obtained as shown in figure 4d, table 7,

Table 8. Experimental estimation of astrometric position errors for an array and a single epoch using the artificial-offset analysis.*

Source	$\Delta\theta_{\text{tro}}$ (μas)		$\Delta\theta_{\text{ion}}$ (μas)		$\Delta\theta_{\text{sta}}$ (μas)		$\Delta\theta_{\text{ins}}$ (μas)		RSS (μas)	
	α	δ	α	δ	α	δ	α	δ	α	δ
G135.28	7	9	1	1	4	2	15	11	17	15
G137.07	34	25	4	1	8	7	14	12	38	28
G200.08	18	19	1	1	8	8	19	20	27	29
G037.50	33	46	6	7	12	12	20	21	41	52
G037.82	41	57	7	8	15	15	20	21	49	63

*Column 1: the source name. Columns 2–9: the position error of the troposphere ($\Delta\theta_{\text{tro}}$), the ionosphere ($\Delta\theta_{\text{ion}}$), the station position ($\Delta\theta_{\text{sta}}$), and the instrument ($\Delta\theta_{\text{ins}}$), in RA (α) and Dec (δ) directions, respectively. The calibration error of each station is 10 mm for the tropospheric zenith delay, 10 TECU (8 mm at 22 GHz) for the ionospheric TEC, 3 mm for the station position, and 0.1 mm for the dual-beam instrumental delay. Columns 10 and 11: the root-sum-square (RSS) of four error sources, i.e., $\text{RSS} = \sqrt{(\Delta\theta_{\text{tro}}^2 + \Delta\theta_{\text{ion}}^2 + \Delta\theta_{\text{sta}}^2 + \Delta\theta_{\text{ins}}^2)}$.

**Fig. 5.** Position error budget of the VLBI astrometry. The value shown in parentheses under the source name is the separation angle between target and reference sources. (Color online)

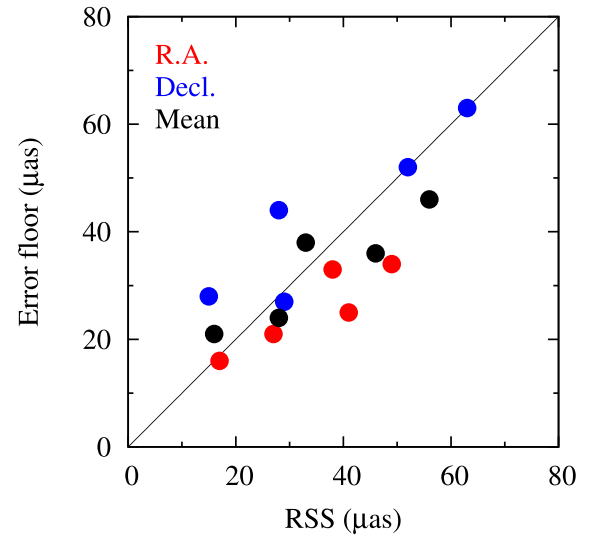
and table 8. The position error is obtained to be 13–20 μas and is constant within a factor of 1.5. It is proportional to the beam size. The position error is given by

$$\Delta\theta_{\text{ins}} \approx \frac{c\Delta\tau_{\text{ins}}}{D}. \quad (5)$$

5.2 Error budget

The position errors caused by the each error source in the calibration were estimated in subsection 5.1 (table 8), while that caused by the thermal noise was estimated in section 4 (table 5). Figure 5 shows the error budget estimated using these position errors. We can find that the position error of the troposphere is much larger than that of the other error sources. In general, the position errors increase with the separation angle, except for the contributions of the thermal noise and the instrument.

We experimentally estimated the position errors of the troposphere, the ionosphere, the station position, and the

**Fig. 6.** Comparison of the astrometric-position error between the experimental estimation (RSS in table 8) and the observational one (the error floor in table 5). The data of five target sources are plotted. The red, blue, and black circles show the errors in RA, Dec, and their geometric mean, respectively. (Color online)

instrument using the artificial-offset analysis. Furthermore, we estimated the error floor, which represents the systematic position error except for the thermal noise contribution, using the post-fit residual of the parallax fitting. We calculated the RSS of the position errors of the four error sources and compared it with the error floor, as shown in figure 6. These are consistent with each other, and the standard deviation of the difference between the RSS and the error floor was calculated to be $\sigma = 10 \mu\text{as}$ in both RA and Dec directions. This consistency suggests that the effect of any other error source is smaller than that of these four error sources.

The error budget shows that the troposphere is the dominant error source, and therefore it strongly affects the error floor. In this case, the error floor is expected to depend on $\Delta \sec Z$. Figure 7 shows the dependence of

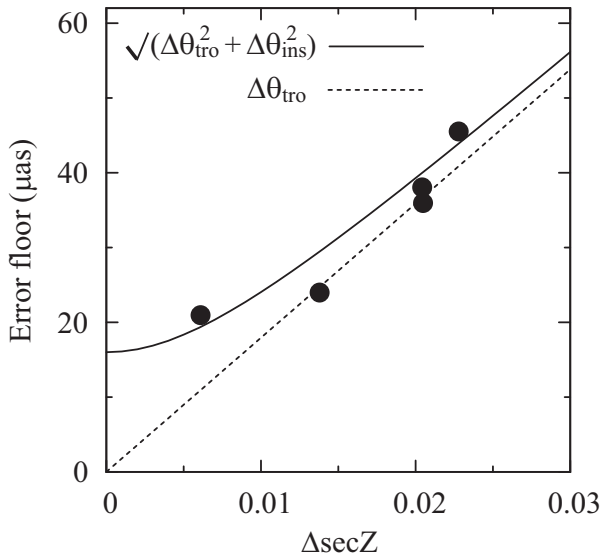


Fig. 7. $\Delta \sec Z$ dependence of the error floor. The data of five target sources are plotted. The dashed line shows the theoretical equation of $\Delta \theta_{\text{tro}} \approx c \Delta \tau_{\text{tro}} / D \cdot \Delta \sec Z \approx 1800 \cdot \Delta \sec Z [\mu\text{as}]$, when the tropospheric zenith delay error is $c \Delta \tau_{\text{tro}} = 20$ mm and the baseline length is $D = 2300$ km. The solid curve shows the root-sum-square of the troposphere and instrument, i.e., $\sqrt{(\Delta \theta_{\text{tro}}^2 + \Delta \theta_{\text{ins}}^2)}$ in the case of $\Delta \theta_{\text{ins}} \approx 16 \mu\text{as}$.

$\Delta \sec Z$ obtained using the $\Delta \sec Z$ in table 2 and the error floor in table 5. We found that the error floor increases in proportion with $\Delta \sec Z$, and could be approximately estimated using equation (2): $\Delta \theta_{\text{tro}} \approx c \Delta \tau_{\text{tro}} / D \cdot \Delta \sec Z \approx 1800 \cdot \Delta \sec Z [\mu\text{as}]$, when the tropospheric zenith delay error is $c \Delta \tau_{\text{tro}} = 20$ mm (Honma et al. 2008b) and VERA's maximum baseline length is $D = 2300$ km. However, note that the contribution of the instrument, which is the second largest error source, cannot be ignored for $\Delta \sec Z \leq 0.01$. This effect of the instrument is almost constant at $\theta_{\text{ins}} \approx 16 \mu\text{as}$ for any source pair (see sub-subsection 5.1.4). The RSS of $\Delta \theta_{\text{ins}} \approx 16 \mu\text{as}$ and $\Delta \theta_{\text{tro}} \approx 1800 \cdot \Delta \sec Z [\mu\text{as}]$, $\sqrt{(\Delta \theta_{\text{tro}}^2 + \Delta \theta_{\text{ins}}^2)}$, as shown in the solid curve in figure 7, is consistent with the error floor for $\Delta \sec Z \leq 0.01$.

For the source pair whose $\Delta \sec Z$ is smaller than 0.01, the error floor is smaller than $25 \mu\text{as}$. Because the monitoring observations of ~ 10 epochs during the observing period of ~ 2 years can statistically reduce the parallax error by a factor of 2–3, compared with the position error in each epoch, we can achieve the parallax precision of the $10 \mu\text{as}$ level. For example, $\Delta \sec Z \leq 0.01$ is provided by a set of the small separation of $\theta_{\text{SA}} \leq 0.5^\circ$ and the high elevation of $\text{EL} \geq 50^\circ$. Among the five target sources, G135.28 satisfies this condition, which is the current best performance of VERA's astrometry.

We further argue that the equation $\Delta \theta_{\text{tro}} \approx 1800 \cdot \Delta \sec Z [\mu\text{as}]$ is also valid for the astrometric position error estimation of lower elevation sources ($\text{EL} < 50^\circ$). We referred to the VERA observations of Orion KL (Nagayama et al.

2020) and Sgr A* (Oyama et al. 2020) as examples of lower elevation sources. The $\Delta \sec Z$ of Orion KL and Sgr A* were calculated to be 0.055 and 0.065, respectively, which are 2–10 times larger than those of the five sources presented in this paper. Their position errors are theoretically estimated using the above equation to be 100 and $120 \mu\text{as}$, respectively. On the other hand, the error floors of Orion KL and Sgr A* are estimated from the post-fit residual of the parallax fitting to be 80 and $130 \mu\text{as}$, respectively (Nagayama et al. 2020; Oyama et al. 2020). These values are consistent with the theoretical values.

5.3 Maser spot structure

The error floor estimated from the post-fit residual is consistent with the RSS of the position errors caused by the troposphere, ionosphere, station position, and instrument at the $10 \mu\text{as}$ level. Therefore, the effect of the maser spot structure would be smaller than $\sim 10 \mu\text{as}$ for our five observed sources. The maser spot structures shown in figure 2 appear to be compact and point-like. The time variations of the peak intensity are smaller than 30% except G137.07. This stable intensity may be related to the stable spatial structure. The position error caused by the maser turbulent motion of 0.5 km s^{-1} is roughly estimated to be $\sim 10\%$ of the parallax (Honma et al. 2010; VERA Collaboration 2020), corresponding to 9– $20 \mu\text{as}$ for our five observed sources. This is consistent with the above estimation.

5.4 Parallax comparison of G135.28

We measured the parallax of G135.28 to be $0.124 \pm 0.011 \text{ mas}$ ($8.1^{+0.8}_{-0.7} \text{ kpc}$). The parallax of this source was also measured by the VLBA H_2O maser observations to be $0.167 \pm 0.006 \text{ mas}$ ($6.0 \pm 0.2 \text{ kpc}$) (Hachisuka et al. 2009). It should be noted that the difference between the two measurements is $0.043 \pm 0.013 \text{ mas}$ (3.3σ), and is statistically significant. The kinematic distance was estimated using a Monte Carlo method to be $7.34^{+1.26}_{-1.51} \text{ kpc}$ (Wenger et al. 2018), which is consistent not only with this work but also with Hachisuka et al. (2009). We cannot estimate the precise parallax of this source using Gaia DR2 (Gaia Collaboration 2018) because of its large error. The parallaxes of the five sources within a $10''$ radius with respect to the H_2O maser position were measured using Gaia DR2 to be 0.79 ± 0.77 , 0.45 ± 2.00 , -0.12 ± 0.48 , 0.40 ± 0.48 , and $-0.13 \pm 0.22 \text{ mas}$.

6 Conclusion

We evaluated the performance of VERA in VLBI phase-referencing astrometry, through the parallax measurements

of five distant star-forming regions. The results are follows:

- (1) The parallaxes of the five star-forming regions were measured to be 0.089–0.200 mas (distances of 5–11 kpc) with 10%–20% uncertainties.
- (2) We created the error budget of the position measurement using the VLBI phase-referencing observations, and found that the troposphere is the dominant error source.
- (3) The position error depends on $\Delta \sec Z$, which can be approximately estimated by $\Delta \theta = c \Delta \tau_{\text{tro}} / D \cdot \Delta \sec Z \approx 1800 \cdot \Delta \sec Z [\mu\text{as}]$. Here, $c \Delta \tau_{\text{tro}} = 20 \text{ mm}$ is the tropospheric zenith delay error and $D = 2300 \text{ km}$ is the maximum baseline length of VERA.
- (4) The parallax precision of $10 \mu\text{as}$ could be achieved for the source pair with $\Delta \sec Z \leq 0.01$ using the current observation and calibration methods of VERA. For example, $\Delta \sec Z \leq 0.01$ is provided by the condition at the close separation of $\theta_{\text{SA}} \leq 0.5^\circ$ and the high elevation of $\text{EL} \geq 50^\circ$.

Acknowledgment

We acknowledge a referee, Dr. Maria Rioja, and an anonymous referee for their valuable comments and suggestions that helped improve our manuscript. Data analysis was [in part] carried out on the Multi-wavelength Data Analysis System operated by the Astronomy Data Center (ADC), National Astronomical Observatory of Japan. TH is financially supported by the MEXT/JSPS KAKENHI Grant Number 17K05398.

References

- Asaki, Y., et al. 2007, PASJ, 59, 397
- Bronfman, L., Nyman, L.-A., & May, J. 1996, A&AS, 115, 81
- Gaia Collaboration 2018, A&A, 616, A1
- Hachisuka, K., et al. 2006, ApJ, 645, 337
- Hachisuka, K., Brunthaler, A., Menten, K. M., Reid, M. J., Hagiwara, Y., & Mochizuki, N. 2009, ApJ, 696, 1981
- Ho, C. M., Wilson, B. D., Mannucci, A. J., Lindqvister, U. J., & Yuan, D. N. 1997, Radio Sci., 32, 1499
- Honma, M., et al. 2003, PASJ, 55, L57
- Honma, M., et al. 2007, PASJ, 59, 889
- Honma, M., et al. 2008a, PASJ, 60, 935
- Honma, M., et al. 2010, Publ. Natl. Astron. Obs. Jpn., 13, 57
- Honma, M., et al. 2012, PASJ, 64, 136
- Honma, M., Tamura, Y., & Reid, M. J. 2008b, PASJ, 60, 951
- Iguchi, S., Kurayama, T., Kawaguchi, N., & Kawakami, K. 2005, PASJ, 57, 259
- Jike, T., Manabe, S., & Tamura, Y. 2009, J. Geodetic Soc. Jpn., 55, 369
- Jike, T., Manabe, S., & Tamura, Y. 2018, J. Geodetic Soc. Jpn., 63, 193
- Kawaguchi, N., Sasao, T., & Manabe, S. 2000, SPIE Proc., 4015, 544
- Kobayashi, H., et al. 2003, in ASP Conf. Ser., 306, New Technologies in VLBI, ed. Y. C. Minh (San Francisco, CA: ASP), 367
- Manabe, S., Yokoyama, K., & Sakai, S. 1991, IERS Tech. Note 8, 61
- Nagayama, T., et al. 2015, PASJ, 67, 65
- Nagayama, T., Hirota, T., Honma, M., Kurayama, T., Adachi, Y., Tamura, Y., & Kanya, Y. 2020, PASJ, 72, 51
- Niell, A. E. 1996, J. Geophys. Res., 101, 3227
- Oyama, T., et al. 2016, PASJ, 68, 105
- Oyama, T., et al. 2020, PASJ, submitted
- Petrov, L. 2016, arXiv:1610.04951
- Pradel, N., Charlot, P., & Lestrade, J.-F. 2006, A&A, 452, 1099
- Reid, M. J., et al. 2019, ApJ, 885, 131
- Reid, M. J., & Honma, M. 2014, ARA&A, 52, 339
- Reid, M. J., Menten, K. M., Brunthaler, A., Zheng, X. W., Moscadelli, L., & Xu, Y. 2009, ApJ, 693, 397
- Reid, M. J., Schneps, M. H., Moran, J. M., Gwinn, C. R., Genzel, R., Downes, D., & Roennaeng, B. 1988, ApJ, 330, 809
- Schaer, S. 1999, Mapping and Predicting the Earth's Ionosphere Using the Global Positioning System, Geod. Geophys. Arb. Schweiz., vol. 59, Inst. für Geod. und Photogram., Zurich, Switzerland
- Shibata, K. M., Kamenno, S., Inoue, M., & Kobayashi, H. 1998, in ASP Conf. Ser., 144, IAU Colloq. 164, Radio Emission from Galactic and Extragalactic Compact Sources, ed. J. A. Zensus et al. (San Francisco: ASP), 413
- Smith, E. K., Jr., & Weintraub, S. 1953, J. Res. Nat. Bur. Stand., 50, 39
- Thompson, A. R., Moran, J. M., & Swenson, G. W., Jr. 2017, Interferometry and Synthesis in Radio Astronomy (Cham: Springer)
- Ulich, B. L., & Haas, R. W. 1976, ApJS, 30, 247
- VERA Collaboration, Hirota, T., Nagayama, T., et al. 2020, PASJ, doi:10.1093/pasj/psaa018
- Wenger, T. V., Balser, D. S., Anderson, L. D., & Bania, T. M. 2018, ApJ, 856, 52
- Wouterloot, J. G. A., & Brand, J. 1989, A&AS, 80, 149